

Effect of Earth-Moon’s gravity on TianQin’s range acceleration noise. II. Impact of orbit selection

Chengjian Luo and Xuefeng Zhang*

*MOE Key Laboratory of TianQin Mission, TianQin Research Center
for Gravitational Physics & School of Physics and Astronomy,
Frontiers Science Center for TianQin, Gravitational Wave Research Center of CNSA,
Sun Yat-sen University (Zhuhai Campus), Zhuhai 519082, China.*

(Dated: October 11, 2022)

The paper is a sequel to our previous work (Zhang et al. Phys. Rev. D 103, 062001 (2021)). For proposed geocentric space-based gravitational wave detectors such as TianQin, gLISA, and GADFLI, the gravity-field disturbances, i.e., the so called “orbital noise”, from the Earth-Moon system on the sensitive intersatellite laser interferometric measurements should be carefully evaluated and taken into account in the concept studies. Based on TianQin, we investigate how the effect, in terms of frequency spectra, varies with different choices of orbital orientations and radii through single-variable studies, and present the corresponding roll-off frequencies that may set the lower bounds of the targeted detection bands. The results, including the special cases of geostationary orbits (gLISA/GADFLI) and repeat orbits, can provide a useful input to orbit and constellation design for future geocentric missions.

I. INTRODUCTION

In ground-based gravitational wave (GW) detectors such as LIGO [1], Virgo [2], and KAGRA [3], Newtonian (or gravity-gradient) noise due to nearby terrestrial gravity fluctuations constitutes a prominent obstacle to sensitivity improvement below ~ 10 Hz [4]. This difficulty on the ground, in addition to seismic noise and the need of long arms (typically $\sim 10^6$ km), has motivated space-based detection in order to access sub-Hertz GW signals [5].

The space-based GW detection missions can be roughly categorized into heliocentric concepts, featured by LISA [6], and geocentric concepts, featured by TianQin [7]. For geocentric missions, though the issue of gravity-field disturbances is expected to be less severe, it may still require careful assessment due to the relative proximity of the satellites to the Earth and the Moon. The goal is to ascertain that there can be a proper separation in the frequencies of gravity-field disturbances and the targeted sensitive frequency bands near mHz, which is prerequisite to a successful space-based GW detection. Unlike ground-based detectors, armlengths of space-based detectors are generally not fixed primarily due to gravitational perturbations to orbital motion. Varying armlengths also induces Doppler shifts (~ 5 MHz) in the beat notes of the inter-satellite heterodyne laser interferometric measurements. The frequency shifts may generate phase ramp-up, onto which GW-induced phase fluctuations are superimposed. The former, containing gravity-field information, should be removed or separated with caution in the pre-data processing stage on the ground. Thereby an accurate simulation of the orbital Doppler shifts would be needed to verify the phase

measurement accuracy and time-delay interferometry [8], at least for TianQin.

The nominal orbit design for TianQin and other geocentric missions should take into account and trade off between a variety of factors [9] such as science objectives, space environment, science payloads, etc. For example, in [10], the impact of orbit selection on the constellation stability of TianQin has been studied, and the permitted ranges of the orbital elements that can meet the payload requirements were identified. In a similar manner, one should also investigate the impact of orbit selection on gravity-field disturbances so as to facilitate trade studies in the orbit design and help seek potential remedies if needed.

In the previous paper [11], we have shown that, with the 1×10^5 km orbital radius and a vertical orbital plane relative to the ecliptic for TianQin, the Earth-Moon’s gravity-field disturbances are dominating in lower frequencies, and roll off rapidly at 1×10^{-4} Hz. The effect does not enter the detection frequency band of $10^{-4} - 1$ Hz where the intersatellite residual acceleration noise requirement of $\sqrt{2} \times 10^{-15}$ m/s²/Hz^{1/2} is imposed, and hence presents no showstopper to the mission. For comparison, the gravity mapping mission GRACE-FO has a much higher roll-off frequency at 4×10^{-2} Hz [12], owing to its low altitude of ~ 500 km above the ground, at which the science instrument can be sensitive to the Earth’s spherical harmonic gravity field to > 150 th degree [13]. Thereby, a separation of 1×10^5 km from the Earth is considered large enough for TianQin to push the gravity-field disturbances out of the detection band.

Nevertheless, these two isolated cases does not tell us much about other possible options in selecting orbital orientations and radii. It begs the questions on how the gravity-field effect changes with different orbit selections, and how one chooses a safe distance from gravity-field noise sources, particularly, the Earth. In this work, we intend to resolve these problems by evaluating the effect

* zhangxf38@sysu.edu.cn

with respect to various inclinations, longitudes of ascending nodes, and orbital radii. The results may provide a useful reference to general orbit and constellation design for geocentric missions, such as GEOGRAWI/gLISA [14], GADFLI [15], B-DECIGO [16], etc.

This is our sixth paper of the concept study series on TianQin’s orbit and constellation [10, 11, 17–19]. For progress on other space environmental effects on TianQin, one may refer to [20–24]. This article is structured as follows. Section II describes the observable and force models used in the simulations. The results are shown in Section III, which also include geostationary orbits, and repeat orbits and resonant orbits are deferred to the Appendices. Finally, we reach the conclusions in Section IV.

II. SIMULATION SETUP

Following [11], we adopt the range acceleration $\ddot{\rho}$ as the observable, which is simply the second time derivative of the range ρ between two satellites. The criteria is to compare the amplitude spectral densities (ASD) of $\ddot{\rho}$ with the residual acceleration noise requirements between two free-floating test masses, which is generally in the order of $10^{-15} \text{ m/s}^2/\text{Hz}^{1/2}$ at mHz. To overcome the insufficiency of double precision, we again use the TQPOP (TianQin Quadruple Precision Orbit Propagator) program [11] to propagate pure-gravity orbits in quadruple precision and with a constant step size of 50 seconds for 90 days. Here the step size is a balanced choice made among the factors of frequency band coverage, numerical accuracy, and computational run-time [11]. Like TianQin, all constellations are assumed to be equilateral triangles barring small deviations, and the three satellites moving in the same nominal circular orbits with 120° phase separation (see, e.g., Table I). The spectral results are not sensitive to the specific year chosen. Without loss of generality, the initial epoch assumes 06 Jun. 2004, 00:00:00 UTC as in [11].

TABLE I. The nominal orbital elements of the TianQin constellation in the J2000-based Earth-centered ecliptic (EarthMJ2000Ec) coordinate system. Here a denotes the semimajor axis, e the eccentricity, i the inclination, Ω the longitude of ascending node, ω the argument of periapsis, and $\Delta\nu$ the difference in the true anomaly.

	a	e	i	Ω	ω	$\Delta\nu$
SC1,2,3	$1 \times 10^5 \text{ km}$	0°	94.7°	210.4°	0°	120°

The detailed force models implemented in TQPOP are summarized in Table II. Further description of them can be found in [11]. In particular, the program offers multiple options in modeling solar system ephemeris, Earth’s precession and nutation, Earth’s static gravity field, etc. The flexibility helps cross-checking model errors, which have been shown not to alter the spectral results for Tian-

Qin [11]. In the following simulations, the more recent options will be used (except for the ocean tides). A new addition to TQPOP lately includes two ocean tide models FES2014b [25] and EOT11a [26]. Based on the results of the test runs, all three models generate spectra consistent with one another in low frequencies. However, since FES2014b contains more high-frequency tidal components (e.g. M6, M8), we will use FES2014b in the following simulation.

TABLE II. The list of force models implemented in TQPOP. If multiple options are given, the first one is used in the simulations.

Models	Specifications
Solar system ephemeris	JPL DE430 [27] JPL DE405 [28]
Earth’s precession & nutation	IAU 2006/2000A [29] IAU 1976/1980 [30]
Earth’s polar motion	EOP 14 C04 [31]
Earth’s static gravity field	EGM2008 ($n = 12$) [32] EGM96 ($n = 12$) [33]
Solid Earth tides	IERS (2010) [29]
Ocean tides	FES2004 ($n = 10$) [34] FES2014b ($n = 10$) [25] EOT11a ($n = 10$) [26]
Solid Earth pole tide	IERS (2010) [29]
Ocean pole tide	Desai (2003) [29]
Atmospheric tides	Biancale & Bode (2003) [35]
Moon’s libration	JPL DE430 [27] JPL DE405 [28]
Moon’s static gravity field	GL0660B ($n = 7$) [36] LP165P ($n = 7$) [37]
Sun’s orientation	IAU [38], Table 1
Sun’s J_2	IAU [38], Table 1
relativistic effect	post-Newtonian [30]

III. SIMULATION RESULTS

We can assess the impact of orbit selection on the gravity-field effect from the changes of the amplitudes A_{kl}^\pm and frequencies f_{kl}^\pm of spectral peaks in the range acceleration ASD curve. The frequencies f_{kl}^\pm can be generally expressed as

$$f_{kl}^\pm = k \cdot f_{orb} \pm l \cdot f_{gra}, \quad (1)$$

where f_{orb} is the satellites’ orbital frequency, and f_{gra} is the intrinsic frequencies of gravity-field disturbances, and k, l are integers.

The goal is to find how the gravity-field effect and the roll-off frequency vary with orbital elements. Here the roll-off frequency refers to where the range acceleration ASD curve intersects the acceleration noise requirement.

The study cases involve three orbital elements, i.e., the inclination i , the longitude of ascending node Ω , and the semimajor axis a . Starting from the nominal orbit of TianQin given in Table I, we vary one single element

at a time to make the trends more prominent. Besides, we discuss the particular case of geostationary orbits in Section III C.

A. Impact of orbital orientations

Orbital inclinations i and longitudes of ascending nodes Ω determine orbital orientations. For single-variable studies, we vary i and Ω separately in the EarthMJ2000Ec coordinate system.

However, due to the existence of obliquity of the ecliptic, the influence of the Earth's static gravity field and its variation with orbital inclinations cannot be fully demonstrated in the EarthMJ2000Ec coordinate system by numerical method. Fortunately, from the previous work [11] (Sec. IVB), we have learned that the total gravity-field effect in terms of the range-acceleration ASD can be roughly divided into two primary parts. The high-frequency part (above $\sim 5 \times 10^{-5}$ Hz) is dominated by the non-spherical gravity field of the Earth, and the low-frequency part (below $\sim 5 \times 10^{-5}$ Hz) is dominated by the Sun and the Moon. Therefore, based on symmetry considerations, we discuss the impact of the Earth's static gravity field with orbital orientations varying in the geocentric equatorial (EarthMJ2000Eq) coordinate system to supplement the effects of all the gravity-field disturbances in the EarthMJ2000Ec coordinate system. Here we mention that there is a 5° difference between the Moon's orbital plane and the ecliptic plane, but it does not contribute significantly to the results.

TABLE III. The orbital elements with different inclinations given in the EarthMJ2000Ec coordinate system at the epoch 06 Jun. 2004, 00:00:00 UTC.

a	i	Ω
1×10^5 km	$0^\circ, 23.5^\circ, 45^\circ, 90^\circ, 135^\circ, 180^\circ$	210.4°

TABLE IV. The orbital elements with different longitudes of ascending node given in the EarthMJ2000Ec coordinate system at the epoch 06 Jun. 2004, 00:00:00 UTC.

a	i	Ω
1×10^5 km	94.7°	$30.4^\circ, 120.4^\circ, 210.4^\circ, 300.4^\circ$

In simulation, setting the orbital radius to a fixed value of 1×10^5 km, we vary the inclination from $i = 0^\circ$ to 180° by $\Delta i = 45^\circ$ intervals (see Table III), where $i = 23.5^\circ$ corresponds to the orbit near the equatorial plane. Then we take four distinct values of longitudes of ascending nodes Ω from 30.4° to 300.4° by $\Delta\Omega = 90^\circ$ intervals (Table IV) in the EarthMJ2000Ec coordinate system. Besides, to supplement the above cases, we vary the inclination from $i_{eq} = 0^\circ$ to 180° by $\Delta i_{eq} = 30^\circ$ intervals (see Table V) in the EarthMJ2000Eq coordinate system.

Due to rotational symmetry, the variation of the Earth's static gravity-field effect with different Ω_{eq} is insignificant, which is also confirmed by our simulations. A few observations can be summarized as follows.

First, the low-frequency peaks of Fig. 1 show that $A_{kl}^-(l \neq 0)$ falls and $A_{kl}^+(l \neq 0)$ rises as i increases, which, for example, can be read from Fig. 2. Moreover, the peaks $k = 1, l = 0$ corresponding to the orbital frequencies coincide with different i 's in the plot. The difference in the amplitudes A_{10} has been discussed in [10].

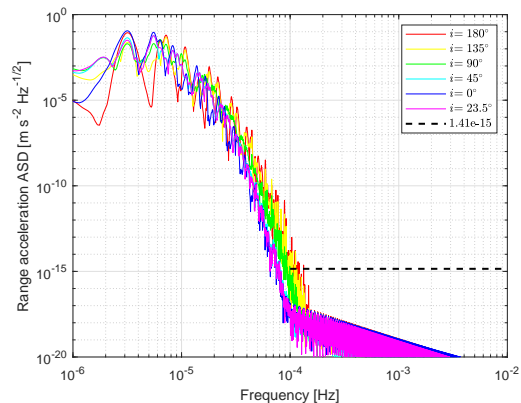


FIG. 1. The range acceleration ASD between SC1 and SC2 calculated with the orbital parameters in Table III, for 90 days with a constant step size of 50 seconds.

TABLE V. The orbital elements with different inclinations given in the EarthMJ2000Eq coordinate system at the epoch 06 Jun. 2004, 00:00:00 UTC, assuming circular orbits and $\Delta\nu = 120^\circ$ for three satellites. Note that $i = 94.7^\circ, \Omega = 210.4^\circ$ (cf. Table I) correspond to $i_{eq} = 74.5^\circ, \Omega_{eq} = 211.6^\circ$.

a	i_{eq}	Ω_{eq}
1×10^5 km	$0^\circ, 30^\circ, 60^\circ, 90^\circ, 120^\circ, 150^\circ, 180^\circ$	211.6°

Second, for high-frequency components, Fig. 1 shows the ASD curves extend to higher frequencies monotonically as i increases from 45° . Besides, Fig. 3 demonstrates that the ASD curves of the Earth's static gravity-field effect extend to higher frequencies as i_{eq} increases. When $0^\circ \leq i \leq 45^\circ$ in the EarthMJ2000Ec coordinate system and $i_{eq} \geq 150^\circ$ in the EarthMJ2000Eq coordinate system, the roll-off frequency is insensitive to changes in inclinations, and hence it does not affect the range of the detection frequency band significantly.

Third, when the satellites are running on the equatorial plane ($i_{eq} = 0^\circ$ and 180°), Fig. 3 also shows the curves' trough values are obviously lower than other cases. This may be attributed to that the satellites experience less "raggedness" of the Earth's gravity field when orbiting in the equatorial plane (see also Fig. 7).

Fourth, compared with the case of orbital inclinations, the gravity-field effect is less sensitive to changes

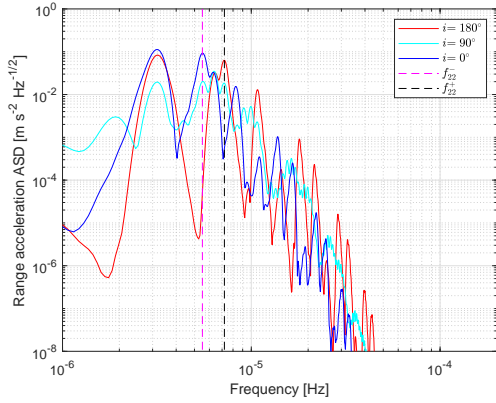


FIG. 2. Examples of low-frequency peaks of Fig. 1 and Eq. 1, where $f_{22}^{\pm} = 2f_{orb} \pm 2f_{moon}$. The plot shows that the amplitude A_{22}^- falls and A_{22}^+ rises as the inclination increases in geocentric ecliptic coordinate system.

of the longitude of ascending node Ω , as shown in Fig. 4. In high frequencies, the differences come from that the Earth's static gravity field varies with Ω in the EarthMJ2000Ec coordinate system because of the obliquity of the ecliptic. In lower frequencies, the differences are partly due to the 5° mismatch between the Moon's orbital plane and the ecliptic plane. The situation is somewhat similar to that of constellation stability [10], which is related to an approximate rotational symmetry about the ecliptic pole.

B. Impact of orbital radii

Based on TianQin, we examine the orbital radius ranging from 4×10^4 km to 1.2×10^5 km by $\Delta a = 2 \times 10^4$ km intervals. For special cases of repeat orbits and resonant orbits, see the appendices. The orbital elements are given in Table VI.

TABLE VI. The orbital elements with different orbital radii given in the EarthMJ2000Ec coordinate system at the epoch 06 Jun. 2004, 00:00:00 UTC.

$a/10^4$ km	$i/^\circ$	$\Omega/^\circ$
4, 6, 8, 10, 12	94.7	210.4

It should be noted that simulations with smaller orbital radii require higher degrees and orders in the Earth's gravity-field model. With estimated gravitational acceleration from different degrees, it is sufficient to set $n = 16$ for $a = 4 \times 10^4$ km, $n = 13$ for $a = 6 \times 10^4$ km, and $n = 12$ for $a \geq 8 \times 10^4$ km [11], so as to meet an accuracy below 10^{-16} m/s²/Hz^{1/2}. The corresponding results of the range acceleration ASD are presented in Fig. 5.

First, with the orbital radius increasing, the ASD curves appear to shift to low frequencies overall. More-

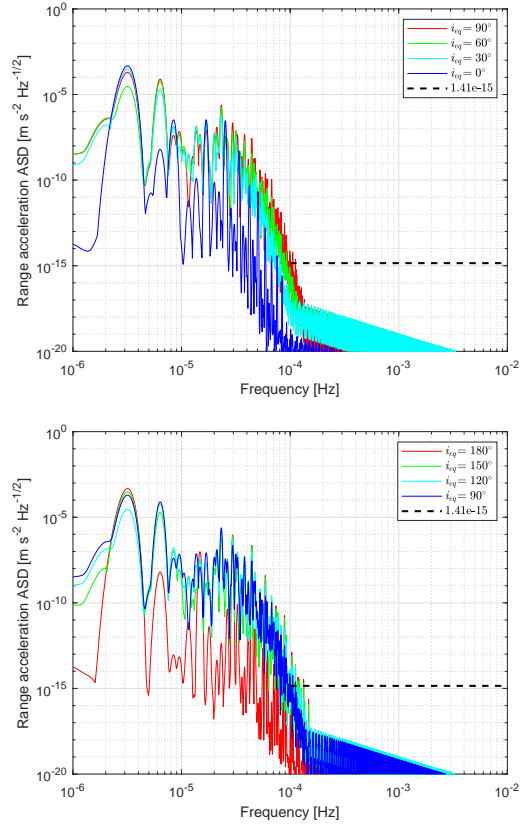


FIG. 3. The range acceleration ASD of the Earth's static gravity field between SC1 and SC2 calculated with the orbital parameters in Table V, for 90 days with a constant step size of 50 seconds.

over, one can read out the roll-off frequencies from Fig. 5, and the values are listed in Table VII and shown in Fig. 6.

Second, one can fit the ASD curves of the range acceleration near the roll-off frequencies f_r by

$$\overline{RA} = \sqrt{2} \times 10^{-15} \times \left(\frac{f_r}{f}\right)^{E_f} \text{ m/s}^2/\text{Hz}^{1/2}, \quad (2)$$

where f is the Fourier frequency, and E_f the power index of the ratio. The fitted values of E_f are given in Table VII. We mention that E_f roughly changes with a^2 and f_r with $1/a^2$.

TABLE VII. The numerical values of the roll-off frequency f_r and the index E_f .

a/km	$f_r/10^{-4}$ Hz	E_f
40000	2.30	21.0
60000	1.46	22.2
80000	1.20	23.8
100000	1.00	26.0
120000	0.93	28.6

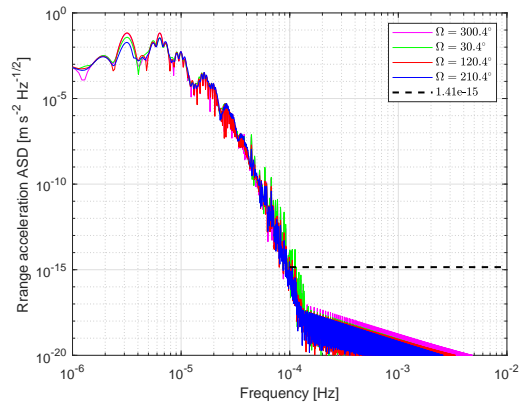


FIG. 4. The range acceleration ASD between SC1 and SC2 calculated with the orbital parameters in Table IV, for 90 days with a constant step size of 50 seconds.

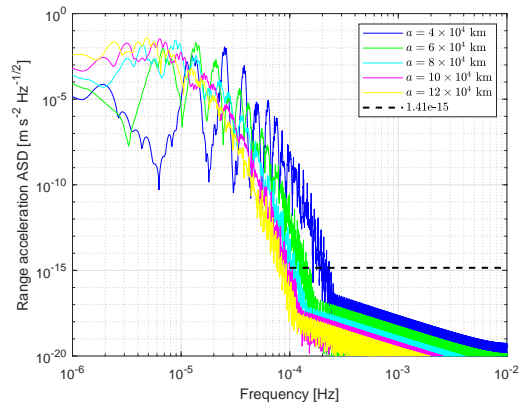


FIG. 5. The range acceleration ASD with different orbital radii from Table VI and for 90 days with a constant step size of 50 seconds.

C. Geostationary orbits for gLISA/GADFLI

In this subsection, we examine geostationary orbits proposed by gLISA/GADFLI. The initial orbital elements are given in Table VIII, which have been optimized for 90 days to stabilize the constellation. Here to focus on the gravity-field effect, we ignore station-keeping maneuvers that may be needed roughly every two weeks [14]. The corresponding range acceleration ASD is presented in Fig. 7, which incorporates the cases with and without the Earth’s non-spherical gravity field in the simulation.

Compared with Fig. 5, the plot shows a rather distinct feature in that the number of peaks is significantly reduced. This is due to the fact that by placing the satellites at the same location above the Earth’s surface, the Earth’s gravity experienced by the satellites becomes localized and nearly static. Therefore, the range acceleration ASD is instead dominated by the Moon and the Sun’s gravity, with the high-frequency components from the Earth’s non-spherical gravity field being suppressed.

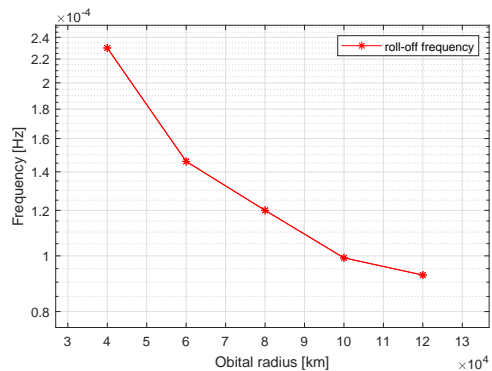


FIG. 6. The relation between roll-off frequency and orbital radius of Fig. 5

This is indicated by the overlapping of the blue and green curves in Fig. 7, where the latter is calculated without the Earth’s non-spherical gravity field in orbit propagation. Moreover, the ASD curve intersects with the noise requirement $3\sqrt{2} \times 10^{-15} \text{ m/s}^2/\text{Hz}^{1/2}$ at $1.69 \times 10^{-4} \text{ Hz}$, which is much lower than the proposed detection frequency band $10^{-2} - 1 \text{ Hz}$ [14].

TABLE VIII. The initial orbital elements of gLISA given in the EarthMJ2000Eq coordinate system at the epoch 06 Jun. 2004, 00:00:00 UTC.

Satellite	a	e	i	Ω	ω	ν^{ini}
SC1	42158.65 km					210.0°
SC2	42164.90 km	0°	0°	0°	0°	330.8°
SC3	42171.00 km					91.3°

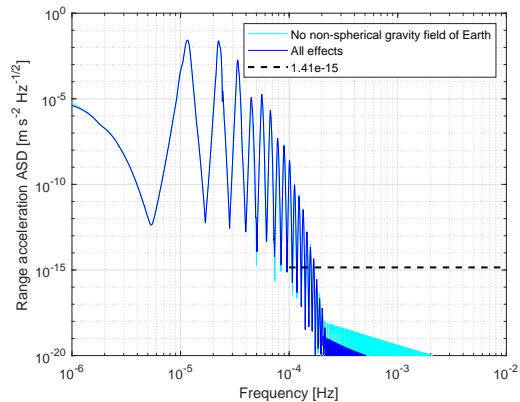


FIG. 7. The range acceleration ASD between two satellites of gLISA/GADFLI, using the orbital parameters in Table VIII, and calculated for 90 days with a constant step size of 50 seconds.

IV. CONCLUSION AND DISCUSSION

In this paper, we have simulated and analyzed the gravity-field effect of the Earth-Moon system on intersatellite range acceleration of geocentric detectors in circular orbits with various orbital orientations and radii. It can help fill the blank in the concept studies of geocentric missions (e.g., [39]) that might have been overlooked. As the previous work has shown [11], one common behavior is that the “orbital noise” dominates in the neighborhood of the orbital frequencies (e.g., 3×10^{-6} Hz for TianQin), and then falls off rapidly below residual acceleration noise requirements ($\sim 10^{-15}$ m/s²/Hz^{1/2}) at specific higher frequencies. Besides, three main conclusions can be drawn here.

First, for a fixed orbital radius 1×10^5 km and the longitude of ascending node 210.4° , the roll-off frequency extends higher frequencies with the inclination increasing when the orbital inclination is greater than 45° in the EarthMJ2000Ec coordinate system. When the inclination is between 0° and 45° in the EarthMJ2000Ec coordinate system or above 150° in the EarthMJ2000Eq coordinate system, the variation of roll-off frequency would not affect the choice of the detection frequency band significantly. For a given inclination, altering the longitude of ascending node has only a small impact.

Second, as the orbital radius increases, the gravity-field effect shifts to lower frequencies so that the detection frequency band can be extended accordingly (cf. Fig. 5).

Third, the gravity-field effect for gLISA in geostationary orbits intersects with the acceleration noise requirement $3\sqrt{2} \times 10^{-15}$ m/s²/Hz^{1/2} at 1.69×10^{-4} Hz. It allows for sufficient clearance from the targeted detection band of $10^{-2} - 1$ Hz [14], and hence presents no showstopper to the mission.

It should be pointed out that the results appear to favor small inclinations (see Section III A). However, for TianQin, the inclination selection is largely driven by other more pressing technical demands. These include spacecraft thermal control [20, 40] and the need of lowering eclipse occurrence [18], etc., which instead favor a 90° inclination. With a vertical orbital plane relative to the ecliptic, setting the radius equal to or greater than 1×10^5 km is sufficient for TianQin to meet the requirement of extending the detection band to as low as 1×10^{-4} Hz. Meanwhile, the upper limit of the orbital radius is likely to be set by the constellation stability requirement [10]. For future work, it would be desirable to develop an analytic model of the orbital dynamics to account for the range acceleration ASD at greater depths.

ACKNOWLEDGMENTS

The authors thank Yuzhou Fang, Lei Jiao, Bobing Ye, Jun Luo, and the anonymous referee for helpful discussions and comments. The work is supported by the National Key R&D Program of China (No.

2020YFC2201202). X.Z. is supported by NSFC Grant No. 11805287.

Appendix: A. Repeat orbits

A repeat orbit has the property that the satellite covers the same ground track periodically. Such orbits may have certain engineering benefits. With the orbital plane facing J0806, we set the orbital periods from one day to four days, and give the initial orbital radii in Table IX. The corresponding results of the range acceleration ASD are presented in Fig. 8. Notably, the ASD of the geosynchronous orbit ($T = 1$ day) bears great resemblance to Fig. 7.

TABLE IX. The initial optimized orbital elements of different repeat orbits for the detectors in the EarthMJ2000Ec coordinate system at the epoch 06 Jun. 2004, 00:00:00 UTC.

T/day	SC1/km	SC2/km	SC3/km
1	42164.14	42162.22	42163.60
2	66934.50	66936.30	66932.00
3	87714.00	87719.70	87710.00
4	106265.00	106278.50	106261.00

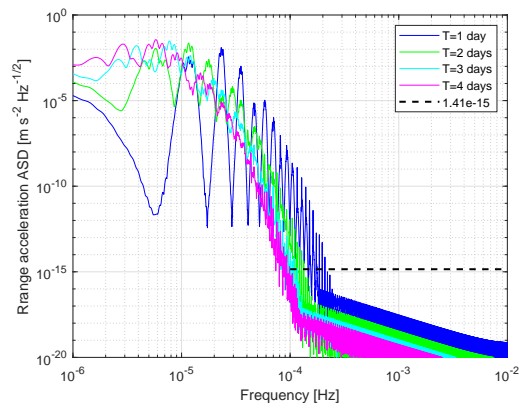


FIG. 8. The range acceleration ASD of different repeat orbital radii between SC1 and SC2, using orbital parameters in Table IX, for 90 days with a constant step size of 50 seconds.

Appendix: B. Resonant orbits

Although for TianQin, the work of [10] has ruled out the orbits resonant with the Moon due to their inferior constellation stability performance. However, the results are still included for the sake of completeness.

We consider orbital period ratios $T_{\text{moon}}/T_{\text{orb}} = 6, 7, 8$. Table X shows the corresponding orbital radii, and the other orbital elements are the same as Table VI. The

TABLE X. The initial orbital elements of different orbital resonance for the detectors in the EarthMJ2000Ec coordinate system at the epoch 06 Jun. 2004, 00:00:00 UTC.

T_{moon}/T_{orb}	SC1/km	SC2/km	SC3/km
8	95796.617	95805.000	95791.000
7	104715.621	104728.000	104710.500
6	116049.338	116070.000	116040.000

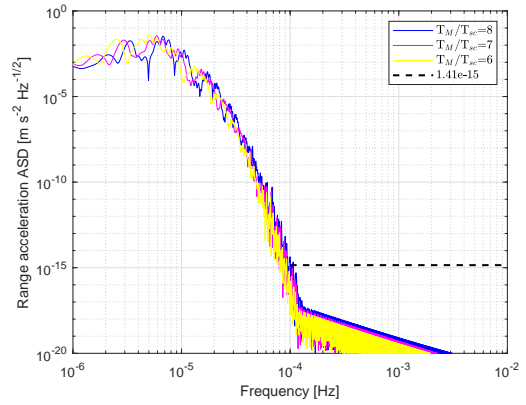


FIG. 9. The range acceleration ASD of different orbital resonance altitude between SC1 and SC2, using the orbital parameters in Table X, for 90 days with a constant step size of 50 seconds.

results are presented in Fig. 9. Compared with non-resonant orbits, the peaks corresponding to the Earth-Moon coupling are enhanced. On the whole, the plot show a similar trend as Fig. 5.

-
- [1] A. Abramovici *et al.*, LIGO: the laser interferometer gravitational-wave observatory, *Science* **256**(5055), 325–333 (1992).
- [2] B. Caron *et al.*, The VIRGO interferometer for gravitational wave detection, *Nucl. Phys. B, Proc. Suppl.* **54**, 167 (1997).
- [3] K. Somiya, Detector configuration of KAGRA - the japanese cryogenic gravitational-wave detector, *Class. Quantum Gravity* **29**, 124007 (2012).
- [4] J. Harms, Terrestrial gravity fluctuations, *Living Rev. Relativ.* **22**, 6 (2019).
- [5] S. Hild, Beyond the second generation of laser interferometric gravitational wave observatories, *Class. Quantum Grav.* **29**, 124006 (2012).
- [6] W. M. Folkner, F. Hechler, T. H. Sweetser, M. A. Vincent, and P. L. Bender, LISA orbit selection and stability, *Class. Quantum Grav.* **14**, 1405 (1997).
- [7] J. Luo *et al.*, TianQin: a space-borne gravitational wave detector, *Class. Quantum Grav.* **33**, 035010 (2016).
- [8] M. Tinto and S. V. Dhurandhar, Time-delay interferometry, *Living Rev Relativ* **24**, 1 (2021).
- [9] X. Zhang, B. Ye, Z. Tan, H. Yuan, C. Luo, L. Jiao, D. Gu, Y. Ding, and J. Mei, Orbit and constellation design for TianQin: progress review, *Acta Scientiarum Naturalium Universitatis Sunyatseni* **60**(1-2), 123 (2021).
- [10] Z. Tan, B. Ye, and X. Zhang, Impact of orbital orientations and radii on TianQin constellation stability, *Int. J. Mod. Phys. D* **29**, 2050056 (2020).
- [11] X. Zhang, C. Luo, L. Jiao, B. Ye, H. Yuan, L. Cai, D. Gu, J. Mei, and J. Luo, Effect of Earth-Moon’s gravity on TianQin’s range acceleration noise, *Phys. Rev. D* **103**, 062001 (2021).
- [12] K. Abich *et al.*, In-orbit performance of the GRACE Follow-on laser ranging interferometer, *Phys. Rev. Lett.* **123**, 031101 (2019).
- [13] R. P. Kornfeld, B. W. Arnold, M. A. Gross, N. T. Dahya, W. M. Klipstein, P. F. Gath, and S. Bettadpur, Grace-fo: The gravity recovery and climate experiment follow-on mission, *Journal of Spacecraft and Rockets* **56**, 931 (2019), <https://doi.org/10.2514/1.A34326>.
- [14] M. Tinto, D. DeBra, S. Buchman, and S. Tilley, gLISA: geosynchronous laser interferometer space antenna concepts with off-the-shelf satellites, *Rev. Sci. Instrum.* **86**, 014501 (2015).
- [15] S. T. McWilliams, Geostationary Antenna for Disturbance-Free Laser Interferometry (GADFLI), arXiv:1111.3708 [astro-ph.IM] (2011).
- [16] S. Kawamura *et al.*, Space gravitational-wave antennas DECIGO and B-DECIGO, *Int. J. Mod. Phys. D* **27**, 1845001 (2018).
- [17] B. Ye, X. Zhang, M. Zhou, Y. Wang, H. Yuan, D. Gu, Y. Ding, J. Zhang, J. Mei, and J. Luo, Optimizing orbits for TianQin, *Int. J. Mod. Phys. D* **28**, 1950121 (2019).
- [18] B. Ye, X. Zhang, Y. Ding, and Y. Meng, Eclipse avoidance in TianQin orbit selection, *Phys. Rev. D* **103**, 042007 (2021).
- [19] M. Zhou, X. Hu, B. Ye, S. Hu, D. Zhu, X. Zhang, W. Su, , and Y. Wang, Orbital effects on time delay interferometry for TianQin, *Phys. Rev. D* **103**, 103026 (2021).
- [20] H. Chen, C. Ling, X. Zhang, X. Zhao, M. Li, and Y. Ding, Thermal environment analysis for TianQin, *Class. Quantum Grav.* **38**, 155015 (2021).
- [21] L.-F. Lu, W. Su, X. Zhang, Z.-G. He, H.-Z. Duan, Y.-Z. Jiang, and H.-C. Yeh, Effects of the Space Plasma Density Oscillation on the Interspacecraft Laser Ranging for

- TianQin Gravitational Wave Observatory, *JGR: Space Physics* **126**, e2020JA028579 (2021).
- [22] W. Su, Y. Wang, C. Zhou, L. Lu, Z.-B. Zhou, T. Li, T. Shi, X.-C. Hu, M.-Y. Zhou, M. Wang, H.-C. Yeh, H. Wang, and P. Chen, Analyses of laser propagation noises for TianQin gravitational wave observatory based on the global magnetosphere MHD simulations, *ApJ* **914**, 139 (2021).
- [23] L. LU, Y. LIU, H. DUAN, Y. JIANG, and H.-C. YEH, Numerical simulations of the wavefront distortion of inter-spacecraft laser beams caused by solar wind and magnetospheric plasmas, *Plasma Sci. Technol.* **22**, 115301 (2020).
- [24] W. Su, Y. Wang, Z.-B. Zhou, Y.-Z. Bai, Y. Guo, C. Zhou, T. Lee, M. Wang, M.-Y. Zhou, T. Shi, H. Yin, and B.-T. Zhang, Analyses of residual accelerations for TianQin based on the global MHD simulation, *Class. Quant. Grav.* **37**, 185017 (2020).
- [25] https://grace.obs-mip.fr/dealiasing_and_tides/ocean-tides/.
- [26] R. Savcenko and W. Bosch, *EOT11a - empirical ocean tide model from multi-mission satellite altimetry*, Tech. Rep. (Deutsches Geodätisches Forschungsinstitut (DGFI), 2012).
- [27] W. M. Folkner, J. G. Williams, D. H. Boggs, R. S. Park, and P. Kuchynka, *The planetary and lunar ephemerides DE430 and DE431*, IPN Progress Report 42-196 (Jet Propulsion Laboratory, 2014).
- [28] E. Standish, *JPL Planetary and Lunar Ephemerides, DE405/LE405*, Tech. Rep. 312.F-98-048 (JPL IOM, 1998).
- [29] G. Petit and B. Luzum, *IERS Conventions (2010)*, Technical Report 36 (BUREAU INTERNATIONAL DES POIDS ET MESURES SEVRES (FRANCE), 2010).
- [30] D. D. McCarthy, *IERS Conventions (1996)*, Technical Report 21 (Central Bureau of IERS - Observatoire de Paris, 1996).
- [31] <http://hpiers.obspm.fr/iers/eop/eopc04/>.
- [32] N. K. Pavlis, S. A. Holmes, S. C. Kenyon, and J. K. Factor, The development and evaluation of the Earth Gravitational Model 2008 (EGM2008), *J. Geophys. Res.* **117**, B04406 (2012).
- [33] F. G. Lemoine, S. C. Kenyon, J. K. Factor, R. Trimmer, N. K. Pavlis, D. S. Chinn, C. M. Cox, S. M. Klosko, S. B. Luthcke, M. H. Torrence, Y. M. Wang, R. G. Williamson, E. C. Pavlis, R. H. Rapp, and T. R. Olson, *The Development of the Joint NASA GSFC and NIMA Geopotential Model EGM96*, Tech. Rep. (NASA Goddard Space Flight Center, 1998).
- [34] F. Lyard, F. Lefevre, T. Letellier, and O. Francis, Modelling the global ocean tides: modern insights from FES2004, *Ocean Dyn.* **56**, 394 (2006).
- [35] R. Biancale and A. Bode, *Mean annual and seasonal atmospheric tide models based on 3-hourly and 6-hourly ECMWF surface pressure data*, STR 06/01 (Geoforschungszentrum Potsdam, 2006).
- [36] A. S. Konopliv, R. S. Park, D.-N. Yuan, S. W. Asmar, M. M. Watkins, J. G. Williams, E. Fahnestock, G. Kruizinga, M. Paik, D. Strelakov, N. Harvey, D. E. Smith, and M. T. Zuber, The JPL lunar gravity field to spherical harmonic degree 660 from the GRAIL primary mission, *J. Geophys. Res. Planets* **118**, 1 (2013).
- [37] A. Konopliv, S. Asmar, E. Carranza, W. Sjogren, and D. Yuan, Recent gravity models as a result of the lunar prospector mission, *Icarus* **150**, 1 (2001).
- [38] B. A. Archinal, M. F. A'Hearn, E. Bowell, A. Conrad, G. J. Consolmagno, R. Courtin, T. Fukushima, D. Hestroffer, J. L. Hilton, G. A. Krasinsky, G. Neumann, J. Oberst, P. K. Seidelmann, P. Stooke, D. J. Tholen, P. C. Thomas, and I. P. Williams, Report of the IAU working group on cartographic coordinates and rotational elements: 2009, *Celest. Mech. Dyn. Astr.* **109**, 101 (2011).
- [39] K. Anderson, R. Stebbins, R. Weiss, and E. Wright, *NASA Gravitational-wave mission concept study final report* (2012).
- [40] X. Zhang, H. Li, and J. Mei, Thermal stability estimation of TianQin satellites based on LISA-like thermal design concept (2018), internal technical report (in Chinese).